

Deep Learning Based 3D Point Cloud Regression for Estimating Forest Biomass

Stefan Oehmcke

University of Copenhagen
stefan.oehmcke@di.ku.dk

Lei Li

University of Copenhagen
Computer Science
lilei@di.ku.dk

Katerina Trepkli

University of Copenhagen
atr@ign.ku.dk

Jaime Revenga

University of Copenhagen
jar@ign.ku.dk

Thomas Nord-Larsen

University of Copenhagen
tnl@ign.ku.dk

Fabian Gieseke

University of Münster
University of Copenhagen
fabian.gieseke@di.ku.dk

Christian Igel

University of Copenhagen
igel@di.ku.dk

Abstract

Quantification of forest biomass stocks and their dynamics is important for implementing effective climate change mitigation measures. The knowledge is needed, e.g., for local forest management, studying the processes driving af-, re-, and deforestation, and can improve the accuracy of carbon-accounting. Remote sensing using airborne LiDAR can be used to perform these measurements of vegetation structure at large scale. We present deep learning systems for predicting wood volume, above-ground biomass (AGB), and subsequently above-ground carbon stocks directly from airborne LiDAR point clouds. We devise different neural network architectures for point cloud regression and evaluate them on remote sensing data of areas for which AGB estimates have been obtained from field measurements in the Danish national forest inventory. Our adaptation of Minkowski convolutional neural networks for regression gave the best results. The deep neural networks produced significantly more accurate wood volume, AGB, and carbon stock estimates compared to state-of-the-art approaches operating on basic statistics of the point clouds. In contrast to other methods, the proposed deep learning approach does not require a digital terrain model. We expect this finding to have a strong impact on LiDAR-based analyses of biomass dynamics.

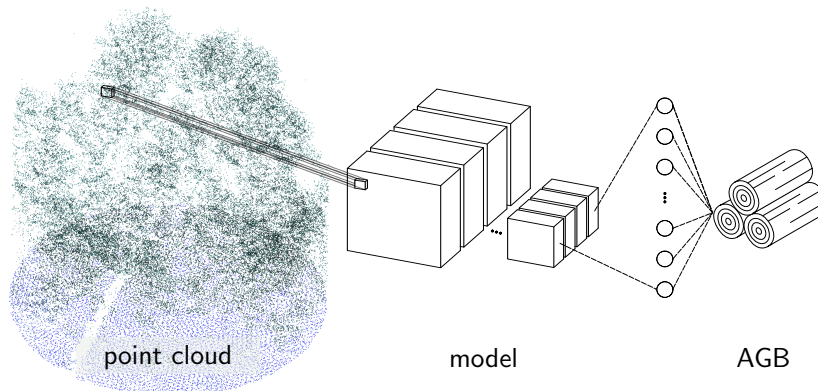


Figure 1: We use point clouds from airborne LiDAR to estimate forest biomass and wood volume using deep learning.

1 Introduction

Robust quantification of forest carbon stocks and their dynamics is important for climate change mitigation and adaptation strategies [FAO and UNEP, 2020]. The Paris Agreement [United Nations / Framework Convention on Climate Change, 2015] and the IPCC [Shukla et al., 2019] acknowledge that climate change mitigation goals cannot be achieved without a substantial contribution from forests. Spatial details in the carbon budget of forests are necessary to encourage transformational actions towards a sustainable forest sector [Harris et al., 2021, 2012]. Currently, many countries do not have nationally specific forest carbon accumulation rates but rather rely on default rates from the IPCC 2018 [Masson-Delmotte et al., 2019, Requena Suarez et al., 2019]), without accounting for finer-scale variations of carbon stocks [Cook-Patton et al., 2020].

Precise spatio-temporal monitoring of forest carbon dynamics at large scales has proven to be challenging [Erb et al., 2018, Griscom et al., 2017]. This is due to the complex structure of forests, topographic features, and land management practices [Tubiello et al., 2021, Lewis et al., 2019]. Technological developments in remote sensing and the concurrent increased availability of field-based measurements have led to an improvement in estimating carbon stocks using remote sensing observations of forest attributes that serve as proxy for above-ground biomass (AGB) [Knapp et al., 2018, Bouvier et al., 2015, Pan et al., 2013].

Currently, three remote sensing techniques are applied to collect data for AGB estimates: i) passive optical imagery, ii) synthetic aperture radar (SAR), and iii) light detection and ranging (LiDAR). Compared to LiDAR, both optical and radar-based data tend to saturate with increasing AGB exceeding 100 Mg ha^{-1} [Mermoz et al., 2015, Sinha et al., 2015, Mitchard et al., 2012]. LiDAR, as an active sensor, can penetrate dense forest canopies regardless of illumination conditions. In comparison, SAR observations are sensitive to topographical variations (e.g., steep slopes or cliffs), while imaging spectroradiometer products are highly dependent on the absence of clouds [Sinha et al., 2015, Treuhaft et al., 2014]. Both alternatives to LiDAR may not be sufficient to detect variations in AGB in the region of interest [Goetz and Dubayah, 2011]. Thus, LiDAR

is the better tool to accurately characterize the fine-scale spatial variability in forest structure and terrestrial carbon stocks [Zhang et al., 2019, Zolkos et al., 2013], but also across broad spatial scales, depending on the platform used (i.e., airborne, drone-based, mobile, and terrestrial laser scanning). Recent developments in spaceborne LiDAR, such as the GEDI mission [Coyle et al., 2019], can be useful for identifying areas with high AGB [Lang et al., 2021]. However, the coarse spatial resolution of these sensors (sparse 25 m footprints in case of GEDI [Hancock et al., 2019]) makes it impossible to derive fine structural information and to produce local as well as sufficiently accurate AGB estimates [Lang et al., 2022, Li et al., 2020, Zhang et al., 2019]. Although airborne laser scanning (ALS) is a better-suited technology for monitoring carbon stock variations over countrywide spatial extents, the quality of the forest AGB prediction can vary depending on the applied method and data resolution [Bouvier et al., 2015, Magnussen et al., 2012].

The state-of-the-art for predicting forest biomass from LiDAR point clouds is to voxelize the data and compute summarizing statistics of the point distribution along the vertical axis, such as mean heights, relative height quantiles, or metrics of heterogeneity [Magnussen et al., 2018, Knapp et al., 2018, d’Oliveira et al., 2012, Stark et al., 2012, Mascaro et al., 2011]. Together with forest attributes obtained from inventory plots, these simple statistical features then serve as inputs to prediction models [Fassnacht et al., 2014] such as linear and non-linear regression, random forests, support vector machines, or neural networks, aimed at predicting the forest characteristics of interest. Based on this approach, several studies are focused on generalizing AGB estimations across different forest types describing different aspects of forest structure at different spatial scales [Bouvier et al., 2015, Asner and Mascaro, 2014, Lefsky et al., 2002]. For instance, Knapp et al. [2020] assessed a variety of LiDAR metrics and auxiliary information (e.g., mean canopy height, maximum possible stand density, maximum possible tree height, vertical canopy heterogeneity, and average wood density) to detect structural forest attributes that may explain stand AGB across different regions. However, in this line of research, assessing the optimal combination of LiDAR metrics that can provide accurate AGB predictions has proven to be a challenging task.

An alternative to manually defining informative features based on summarizing point clouds statistics is to use deep learning [LeCun et al., 2015] approaches that directly work on point clouds [Guo et al., 2020]. Deep learning on point clouds for regression, however, is an almost unexplored learning setting, except for the estimation of geometric properties from point clouds (e.g., hand pose-estimation [Ge et al., 2018, Frintepe et al., 2021]) and bounding box prediction in general detection tasks [Zhou and Tuzel, 2018, Qi et al., 2019]. In addition, ALS, a technology with peculiarities [Næsset, 2009, Goodwin et al., 2006], produces more challenging point clouds than most standard benchmark data sets for point cloud tasks, since they are measured from the top instead of from the ground, and the corresponding point densities are usually lower compared to those induced by other LiDAR-based technologies (e.g., TLS or drone-based LiDAR). The applicability of a deep learning system to estimate crop biomass has also been tested more recently using point clouds from LiDAR mounted on a roving vehicle [Pan et al., 2022] in a small scale experiment.

This study brings forward deep learning systems to improve forest biomass and wood volume quantification based on airborne LiDAR data with high spatial

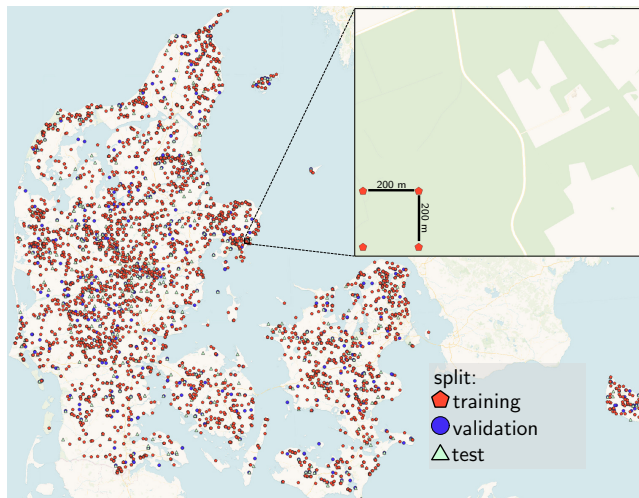


Figure 2: Measurement sites (Danish NFI plots). Color indicates how the data were split into training, validation, and testing (map background based on [Open-MapTiles \[2023\]](#) and [CARTO \[2023\]](#)).

resolution per sample (0.07 ha). Specifically, we propose to apply deep neural networks directly to the point clouds (see Fig. 1) instead of relying on models being based on simple statistical features (we presented the initial idea as a poster in [Oehmcke et al. \[2022\]](#)). We hypothesize that maintaining the full dimensions of the point cloud, and hereby preventing the information loss associated with reducing dimensionality into a few statistical features strengthens predictions. The experimental evaluation shows that predictions using deep learning are considerably more accurate than currently employed methods. Further, in contrast the currently employed methods, our approach requires neither a digital terrain model (DTM) nor a CHM. This may pave the way for a paradigm shift for LiDAR-based analyses of biomass dynamics.

2 Methods

In the following, we first introduce the data used in this study in Section 2.1, which combines field-based biomass and wood volume measurements with ALS point clouds. Afterwards, in Section 2.2 the assessed deep learning architectures are presented along with their required adjustments for point cloud regression. The established baseline methods, which rely on statistics derived from the point clouds are discussed in Section 2.3. Finally, we give details on why and how to correct the bias for least-square regression tasks in Section 2.4.

2.1 Forest Data

This section gives details on the two used data sources and their processing. First, the inventory data of AGB and wood volume are described, as well as how they were collected. Then, we report on the LiDAR data linked to these measurements.

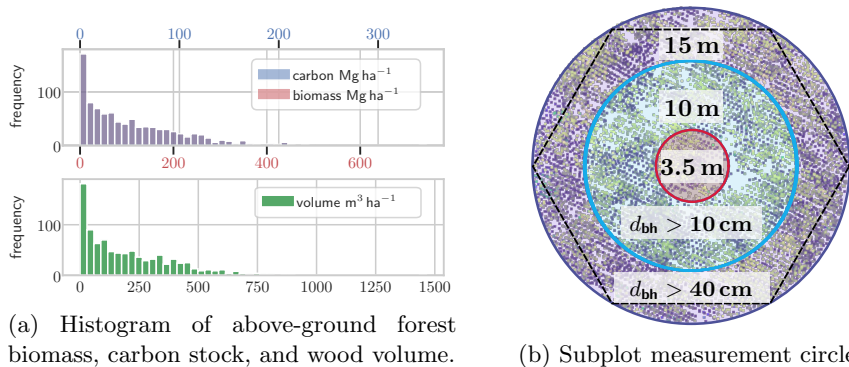


Figure 3: The left plot (a) shows the distribution of target variables. Above-ground biomass and carbon stocks overlap completely since the carbon stock estimate is computed as a linear function of the biomass. The right plot (b) shows exemplary input point cloud (top view of a single subplot) and a representation of the measurement circles. The dashed hexagon encloses the points used by the deep learning point cloud methods.

2.1.1 Forest Inventory

The volume (in $\text{m}^3 \text{ha}^{-1}$) and biomass (Mg (metric ton) ha^{-1}) estimates used to train and evaluate the deep learning models stem from the Danish National Forest Inventory (NFI), see Fig. 3a for their distribution. The Danish NFI is based on a grid with cells of size 2×2 km covering the entire land surface of the country [Nord-Larsen and Johannsen, 2016]. A plot is composed of four circular subplots with a radius of 15 m. Each subplot is located in the corners of a 200×200 m square, which is randomly placed within each grid cell (Fig. 2). The full set of plots is geographically partitioned into five spatially balanced interpenetrating panels [Kish, 1998, McDonald, 2003, Olsen et al., 1999, Zhang et al., 2003]. Each year within a 5-year cycle, a different panel is measured, representing one fifth of the total set but representative of the entire country. These labeled data used in our study range from 2013 to 2017.

In the Danish NFI, each subplot is composed of three concentric circles with radii of 3.5 m, 10 m, and 15 m, respectively. Following standard procedures, a single caliper measurement of diameter is made at breast height (d_{bh}) (i.e., 1.3 m from the ground) for all trees in the 3.5 m circle. Trees with d_{bh} larger than 10 cm are measured in the 10 m circle, and only trees with d_{bh} larger than 40 cm were recorded in the 15 m circle (see Fig. 3b). For a random sub-sample, further measurements of the total height (h), crown height (h_c), age, and diameter at stump height (d_{st}) of two to six trees within each subplot are also obtained.

Based on the sub-sample measured for both h and d_{bh} , models were developed for each species and growth region. These models are based on the observed mean height and mean diameter within each subplot for creating localized regressions using the approach suggested by Sloboda et al. [1993]. For subplots where no height measurements were available, generalized regressions were developed based on a modified Näslund-equation [Näslund, 1936, Johannsen, 1999]. Subsequently, individual tree volume and biomass were estimated using species-specific models [Nord-Larsen et al., 2017a]. Since trees were measured

in different concentric circles depending on their diameter, the volume of growing stock and biomass in each subplot were calculated by scaling the estimated AGB and wood volume of each tree according to the circular area in which the tree was measured. Carbon stocks can be considered as a linear function of the forest biomass, thus, in this study was not used as a separate regression target.

2.1.2 Point Cloud Data

Airborne LiDAR point cloud data covering the whole of Denmark from 2014 to 2018 are publicly available from the Danish *Agency for Data Supply and Efficiency* (<https://dataforsyningen.dk>). Specifically, a sampling campaign in 2014 and 2015 covered the entire country, while a fifth of the country was again scanned in 2018 (in eastern Jutland and Funen). The average resolution of the point clouds was reported to be 4.5 points per m² with a vertical and horizontal point accuracy (given as root mean squared error (RMSE)) of 5 cm and 15 cm, respectively. We extracted the point clouds corresponding to the subplots studied in the NFI (see Fig. 4). The average number of points per subplot equaled 11 684 with a standard deviation of 6743 points.

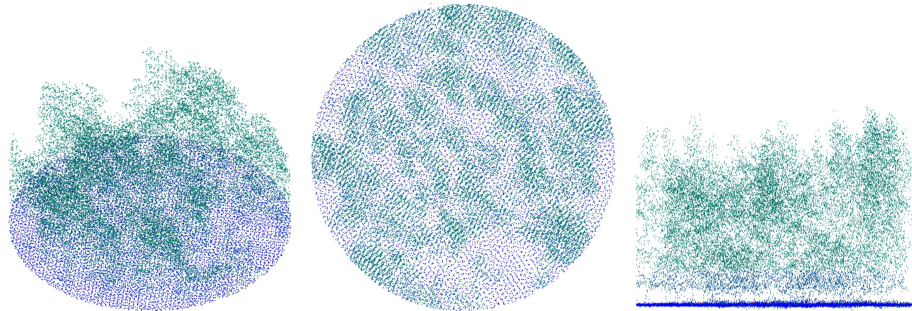
2.1.3 Preprocessing

Several preprocessing steps were conducted for both the deep neural networks (operating on the point clouds) as well as for the baseline models that operate on simple statistical features.

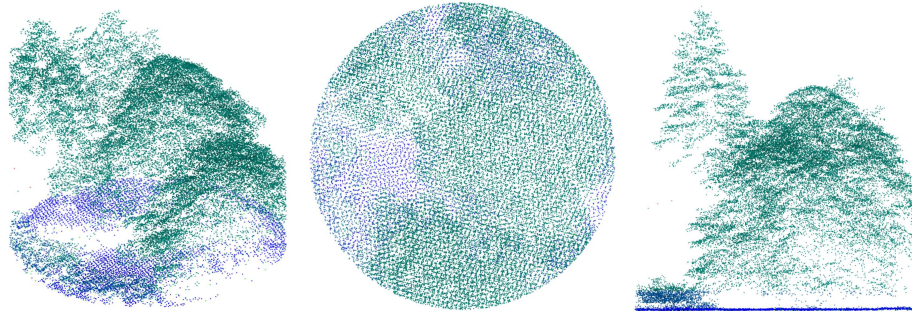
For the plot-specific point clouds, the NFI identified four types of errors. In the first type, trees visible in the point cloud do not belong to the field-based measurements but reach into the plot from the outside, while in the second type non-forest objects, such as land-lines or buildings, are part of the point cloud. We chosen not to exclude these data since a method that directly works with the point cloud should detect irrelevant parts by itself, meaning that some previously excluded data should now be usable. The third error type occurs when the plot had been harvested in-between field measurements and airborne point cloud acquisition. Finally, the fourth error type consisted of unreasonable values. Since the third and fourth error flags are intractable, the samples were excluded from the model training. In addition, all samples with no points above 1.3 m were removed, as this was the minimal height considered for the biomass measurements¹.

The remaining dataset consists of $M = 6101$ individual point clouds, each being labelled with a corresponding biomass and wood volume measurement as described in Sec. 2.1. The biomass and wood volume were measured at different times than the collection of point clouds. To ensure that both data sources matched, we only considered point clouds observed within one year of the biomass measurement for our validation and test set. For training, we took larger temporal gaps (up to nine years) into account and added the time interval in years as a feature to the point clouds. Since some sites were measured multiple times, we kept measurements from the same site together in either training, validation, or test datasets (i.e., no site/plot considered during training or for validation occurred in the test set).

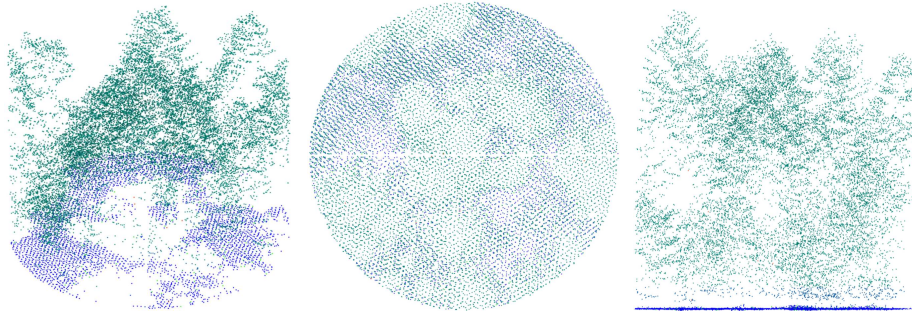
¹Keeping these samples would simply reduce the errors, because they could be handled by a simple rule that predicts zero if the maximum height is below 1.3 m.



(a) Broadleaf only subplot with AGB of 27.93 Mg ha^{-1} .



(b) Mixed forest subplot (28% conifer) with AGB of $226.50 \text{ Mg ha}^{-1}$.



(c) Conifer only subplot with AGB of $150.59 \text{ Mg ha}^{-1}$.



Figure 4: Examples of subplots with different fractions of broadleaf and conifer trees. Green and blue indicate points classified belonging to trees and ground, respectively. We show three perspectives: isometric front, top, and side view.

Finally, to train, validate and test all the models, we split the data as follows: the training set contains 3232 samples with a time interval of more than one year and 1039 samples with an even longer time interval (i.e., 4271 training samples in total). The validation set consists of 919 and the test sets of 911 samples with a maximum distance of one year between paired point cloud and biomass measurements.

2.2 Deep Regression for Point Clouds

From a mathematical perspective, a single point cloud can be represented via a set $\mathcal{P} = \{\mathbf{x}_1, \dots, \mathbf{x}_{n_{\mathcal{P}}}\} \subset \mathbb{R}^N$, where $n_{\mathcal{P}}$ is the number and N the dimensionality of the points (typically, $N = 3$). Besides these coordinates, additional information is often provided for each point, such as color or intensity. These features paired with the points define the set

$$\mathcal{P}_{\mathcal{F}} = \{(\mathbf{x}_1, \mathbf{f}_1), \dots, (\mathbf{x}_{n_{\mathcal{P}}}, \mathbf{f}_{n_{\mathcal{P}}})\} \subset \mathbb{R}^N \times \mathbb{R}^D \quad (1)$$

with $\mathbf{f}_i \in \mathbb{R}^D$ containing the additional features. Such a point cloud is given for each instance (e.g., one subplot corresponds to one point cloud, see Fig. 4). The point cloud sets typically have different cardinalities and are unordered. Accordingly, the output of a model should not depend on the order of the provided points, a property referred to as permutation invariance. Furthermore, the spatial structure of such point clouds can be highly irregular and the density of points is typically very sparse (such characteristics usually vary among different regions as well).

Compared to deep convolutional neural networks (CNNs) for standard 2D and 3D images, the research field of deep learning for point cloud data has yet to mature. There are several approaches for adapting neural networks for point cloud processing, differing among others in how they deal with the key questions of how to extend the concept of spatial convolutions to sparse point clouds. Most deep learning systems for point clouds are developed for segmentation and other classification tasks [Hackel et al., 2017, Chang et al., 2015, Wu et al., 2015]. In this study, we focused on regression tasks. We adapted and compared three widely-used and conceptually different point cloud classification approaches for regression: the classic PointNet [Qi et al., 2017], the kernel point convolution (KPConv) [Thomas et al., 2019], and a Minkowski CNN [Choy et al., 2019].

We extended the open-source library Torch-Points3D [Chaton et al., 2020] to support regression and will contribute our networks and anonymized dataset to the library upon acceptance of this manuscript.

2.2.1 PointNet

The seminal PointNet is one of the first deep learning architectures developed for point clouds [Qi et al., 2017]. PointNet-type networks apply the same weight matrices to each input point. That is, the resulting feature maps are defined by a shared (dense) neural network. The original architecture is based on the use of multiple such neural network blocks. In between these blocks, input/feature transformations are used to align the data via learnable transformation matrices. At the end, to facilitate a variable number of points and to achieve permutation invariance, a symmetric set function is applied, which can be simply a global

max-pooling operation. Two PointNet variants have been proposed in the seminal work to address classification and segmentation scenarios, respectively.

To adapt the architecture for regression, we adopted the classification PointNet architecture up to the global feature aggregation. We then replaced the subsequent two hidden fully-connected layers (output dimensionalities: 512-256) with three fully-connected layers (output dimensionalities: 512-256-128) and considered a final linear output layer.

2.2.2 KPConv

The kernel point convolution [Thomas et al., 2019] extends standard discrete convolution to the domain of point clouds. Kernel point convolutions consider, for a given input point $\mathbf{x} \in \mathbb{R}^N$, a local neighborhood along with points called kernel points that are used to define a convolution operator. More precisely, $\mathcal{P}_{\mathcal{F}}$ is convolved by a kernel g at a point $\mathbf{x} \in \mathbb{R}^N$ is defined via

$$(\mathcal{P}_{\mathcal{F}} * g)(\mathbf{x}) = \sum_{(\mathbf{x}_i, \mathbf{f}_i) \in \mathcal{N}_{\mathbf{x}}} g(\mathbf{x}_i - \mathbf{x}) \mathbf{f}_i . \quad (2)$$

Here $\mathcal{N}_{\mathbf{x}} = \{(\mathbf{x}_i, \mathbf{f}_i) \in \mathcal{P}_{\mathcal{F}} \mid \|\mathbf{x}_i - \mathbf{x}\| \leq r\}$, where $r \in \mathbb{R}^+$ is a hyper-parameter defining the domain $\mathcal{B}_r^N = \{\mathbf{y} \in \mathbb{R}^N \mid \|\mathbf{y}\| \leq r\}$ of the kernel g . The kernel g is based on a set $\{\tilde{\mathbf{x}}_1, \dots, \tilde{\mathbf{x}}_K\} \subset \mathcal{B}_r^N$ of K kernel points, where each kernel point $\tilde{\mathbf{x}}_k$ has an associated weight matrix $W_k \in \mathbb{R}^{D_{\text{in}} \times D_{\text{out}}}$, which maps a feature vector $\mathbf{f} \in \mathbb{R}^{D_{\text{in}}}$ to a new feature vector $\mathbf{f}' \in \mathbb{R}^{D_{\text{out}}}$ (for the first such convolution layer, we have $D_{\text{in}} = D$). One option for the kernel $g : \mathcal{B}_r^N \rightarrow \mathbb{R}^{D_{\text{in}} \times D_{\text{out}}}$ is

$$g(\mathbf{y}) = \sum_{k=1}^K h(\mathbf{y}, \tilde{\mathbf{x}}_k) W_k , \quad (3)$$

where $h = \max(0, 1 - \frac{\|\mathbf{y} - \tilde{\mathbf{x}}_k\|}{\sigma})$ and $\sigma \in \mathbb{R}^+$ is a user-defined model parameter [Thomas et al., 2019]. Thus, the kernel yields a weighted sum of weight matrices and each kernel is parameterized by its own kernel points and the corresponding weight matrices. The weight matrices are learnt similarly to the coefficients of convolution operators in standard CNNs. The kernel points can either also be learnt (“deformable”) or can be fixed (“rigid”) systematically around the center of \mathcal{B}_r^N [Thomas et al., 2019]. Pooling operations are realized via creating a 3D grid in which all points in a cell are aggregated (see Sec. 2.2.3).

We adapt the KPConv architecture proposed for classification (KP-CNN) to utilize it for regression. KP-CNN follows the structure of ResNet, thus modifying it for regression was straightforward and was achieved by changing the output layer to have the identity as activation function. We resorted to fixed kernel points since deformable ones consistently performed worse on our dataset.

2.2.3 Minkowski Convolutional Neural Network

A straightforward approach to process point clouds is to voxelize the points to a 3D image (with D channels) and to apply a standard 3D convolutional neural network (CNN) to the resulting image. This requires binning, but while a coarse binning may discard important information, a fine-grained binning can render the computations intractable. However, the points are typically very sparse in 3D space. This lends to keeping a sparse representation and

applying spatially sparse 3D convolutions, which basically operate only in areas where points exist [Graham, 2015, Graham et al., 2018]. A state-of-the-art implementation of sparse convolutions for point clouds is given by the Minkowski Engine, an auto-differentiation library, which allows to efficiently implement standard architectures, such as ResNet with 3D convolutions [Choy et al., 2019].

Both the Minkowski and KPConv architectures progressively downsample the point cloud based on a 3D grid via pooling operations. The initial grid size is only bound to the horizontal and vertical accuracy of the point data, meaning that a too small grid size cannot be processed efficiently. Therefore, it is crucial to set the initial grid size according to the data and task. The subsequent pooling steps are then based on this initial size and work similarly to standard 2D pooling operations. Once a grid is created, a voxel-based approach, such as Minkowski CNNs, aggregates all voxels within a grid cell to a new voxel. In contrast, KPConv takes the mean of the position of all points within a cell to form a new point. By doubling the size of the grid cells in each subsampling/pooling layer, the number of points/voxels is gradually reduced, corresponding to an increase in the size of the receptive field. The features associated with each new point can be obtained, for example, via max-pooling (applied to the feature vectors of the pooled points) or by applying the chosen convolution operator.

Using the Minkowski Engine library, we built two 3D versions of SENet (SENet14 and SENet50) for regression [Hu et al., 2018], see Fig. 5. To that end, we replaced 2D convolutions with their 3D equivalent. The stride of the initial convolution of SENet was changed from 2 to 1 in order to avoid early loss of information. We also replaced Rectified Linear Unit (ReLU) activation functions with Exponential Linear Units (ELU) [Clevert et al., 2016]. Finally, the output layer was changed to fit the number of target variables and does not apply a non-linear activation. The two network versions differ in the number of trainable parameters as shown in Tab. 1 and are referred to as MSENNet14 and MSENNet50, respectively.

2.2.4 Experimental Setup for Forest Attribute Regression

Three different neural network architectures were applied: the proposed regression versions of PointNet, KPConv, and two 3D version of SENet (MSENNet14 and MSENNet50) built with the Minkowski Engine. All code was written in Python and PyTorch [Paszke et al., 2019] and trained on A100 GPUs. The positions of the input points were given in the projected coordinate system EPSG:25832. We centered the x -, y -, and z -coordinates for each subplot individually to get a local reference frame. Scaling was applied by dividing by 15, 15, 20 m, respectively, so that the coordinates lie within $[-1, 1]$ for the x - and y -coordinates. We do not need to calibrate our model using a DTM, as is required by state-of-the-art methods based on point cloud statistics.

We tuned the initial grid size of KPConv and the MSENNet models by gradually decreasing it (i.e., increasing the spatial resolution) until no improvement could be seen on the validation set. Both architectures worked best with the initial grid size set to 0.025. The number of trainable model parameters and runtimes are given in Tab. 1.

To increase diversity in the training set, several augmentations were considered. First, a random rotation around the z -axis was applied. We did not consider rotating the x - and y -axis since a tilt would result in unrealistic samples

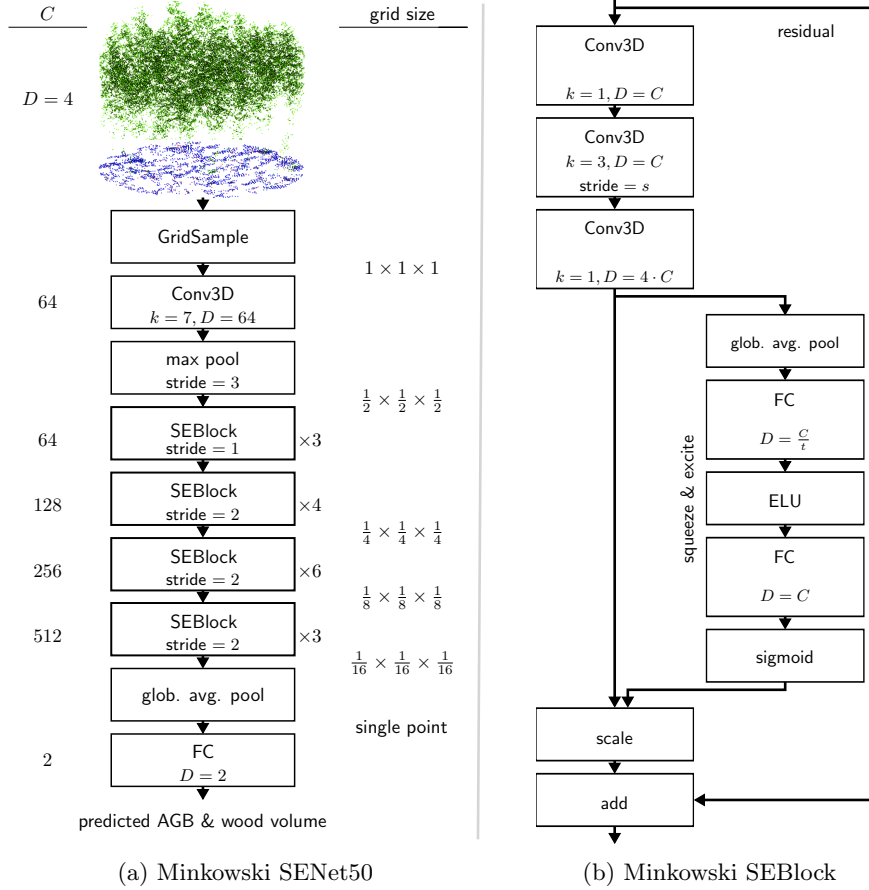


Figure 5: (a) Implemented Minkowski SENet50 (MSENet50) architecture. The grid sizes are relative to the initial grid size. Conv3D refers to sparse 3D convolution with D channels followed by ELU activation and batch normalization. The kernel size k and stride are given as single numbers but extend to all three dimensions (e.g., $3 = 3 \times 3 \times 3$). FC layers are fully connected layers of dimensionality D . (b) Bottleneck block, parameterized by its input size C , stride s , and reduction rate t (defaults to 16).

Table 1: Number of trainable parameters and average runtime (elapsed real time using a single GPU) for one pass through the test set as well as the total training time for the point cloud models.

Model	number of parameters	test time	train time
PointNet	3 503 691	7s	7h
KPCConv	12 287 232	55s	42h
MSENet14	14 403 966	4s	4h
MSENet50	48 716 722	5s	9h

(e.g., change of growth direction). Thereafter, random dropout of points with a dropout rate of 20% in 50% of all samples was applied, which increases variety and simulates changes in point density. Finally, each dimension of the point position was shifted by adding a small random value drawn from a zero-mean truncated Gaussian distribution with variance 0.001 and support $[-0.05, 0.05]$.

One goal was to create precise wood volume and above-ground biomass maps over large areas. Therefore, instead of using the entire circle in which the measurements were taken, we resorted to a hexagonal shape in the x- and y-coordinate, see Fig. 3b. This approach facilitates an easy tiling of large areas without gaps and overlaps. The hexagonal shape covers almost all of the points, in particular those in the inner circles (in control experiments, we verified that considering the whole subplot does not lead to a significant performance increase).

We employed the AdamW [Loshchilov and Hutter, 2019] optimizer with weight decay set to 0.01. The initial learning rate was 0.001, which was adapted according to the cosine annealing schedule with warm restarts ($T_0 = 10, T_{\text{mult}} = 2$) [Loshchilov and Hutter, 2017] for 310 epochs. The batch size was 32 and the smooth L1 function Girshick [2015] was used as training loss. These hyperparameter configurations were chosen based on the highest R^2 score on the validation set. The input channel was filled with ones to encode the presence of a point.

2.3 Baseline Methods

The baseline models considered in this study for estimating above-ground biomass, rely on precomputed features from the normalized height distribution in accordance with Nord-Larsen et al. [2017b]: mean height, height standard deviation, coefficient of variation, skewness, kurtosis, percentiles of the height distribution (5th, 10th, 25th, 50th, 75th, 90th, 95th, 99th), and the interception ratio (IR), which is the fraction of points above one meter compared to all first returns. For each point cloud sample, these features except the IR were computed twice, once for all points and once only for the points 1 m above ground. To determine the height of a point relative to the ground, we calibrated it semi-automatically, using two DTMs with different spatial resolutions (25 m² and 5 m²), and the first return of each light pulse from the airborne LiDAR, following the study of Magnussen et al. [2018]. In preliminary analysis, it was observed that this approach led to better results than using all the recorded returns from each LiDAR-derived light pulse. In contrast, the deep learning methods simply use

all the information included in the point clouds without the need to filter out the point cloud datasets according to the number of returns. In total, $d = 28$ statistical features were extracted for each point cloud sample.

2.3.1 Linear and Power Regression

The first two baseline methods were linear regression and power regression models. For the linear regression models, all the d features were used as explanatory variables. The multivariate power regression can be regarded as the state-of-the-art for predicting AGB, above-ground carbon stocks, and tree volume from the point cloud features [Magnussen et al., 2018]. Following Magnussen et al. [2018], we fitted models of the form

$$y = w_1 \cdot z_{\text{mean AG}}^{w_2} \cdot z_{95^{\text{th AG}}}^{w_3} \cdot \text{IR}^{w_4} \quad (4)$$

for each quantity of interest. Here, $z_{\text{mean AG}}$ is the mean height of the points one meter above ground, $z_{95^{\text{th AG}}}$ is the 95th percentile of the height distribution of point one meter above ground, and IR is the inception ratio. For each model, the parameters $w_1, \dots, w_4 \in \mathbb{R}$ were set to the optimal least-squares estimates.

2.3.2 Random Forest

We trained random forest (RF) models with 5000 trees [Breiman, 2001] and resorted to the popular Scikit-Learn implementation [Pedregosa et al., 2011]. The out-of-bag (OOB) error was used to tune the RF hyper-parameters. We considered $\{0.1, 0.2, \dots, 1\}$ for the ratio of features to consider at every split, $\{0.1, 0.2, \dots, 1\}$ for the ratio of samples to consider for each tree, $\{5, 6, \dots, 20, \infty\}$ for the maximum tree depth, and $\{1, 2, 4, \dots, 16\}$ for the minimum number of samples required at each leaf node. The best model used 90% of the features at every split, 20% of the training data for each tree, had a maximum depth of 11, and required a minimum number of 6 samples at each leaf node.

2.4 Bias Correction

Least-squares regression with deep learning models typically lead to biased models in the sense that the sum of residuals on the training data set is not zero [Igel and Oehmcke, 2022]. Consider a regression model $\mathbb{R}^d \rightarrow \mathbb{R}$ of the form

$$f(\mathbf{x}) = \mathbf{a}^T h_\theta(\mathbf{x}) + b \quad (5)$$

with parameters (θ, \mathbf{a}, b) . Here $h_\theta : \mathbb{R}^d \rightarrow \mathbb{R}^m$ for some positive integer m , $b \in \mathbb{R}$, $\mathbf{a} \in \mathbb{R}^m$, $\mathbf{x} \in \mathbb{R}^d$. This model can be a deep neural network, where all layers but the final layer are represented by the function h_θ and the parameters θ comprise all weights except those in the final layer. Training a deep neural network for regression using iterative optimization with mini-batches and stopping after a fixed training time or based on performance on a hold-out data set cannot be expected to choose the parameter b in a way that the residuals on the training data sum to zero. That is, on the training data $\{(\mathbf{x}_1, y_1), \dots, (\mathbf{x}_N, y_N)\}$ we have $\sum_{i=1}^N (y_i - (\mathbf{a}^T h_\theta(\mathbf{x}_i) + b)) \neq 0$. This can introduce a systematic error that accumulates if we are interested in the total aggregated performance over many data points. We therefore used the method proposed by Igel and Oehmcke [2022] to correct this bias by replacing b by

Table 2: Comparison of methods showing the R^2 score, RMSE, and MAPE on the test set. The R^2 and MAPE for biomass are the same as for carbon stocks. Note that we excluded 0 biomass measurements from MAPE to avoid numerical issues. The median (med.) and best result of 5 trials are shown, the best results are highlighted.

target	model	R^2		RMSE		MAPE	
		med.	max	med.	min	med.	min
AGB	linear	0.757	0.757	49.88	49.88	577.78	577.78
	power	0.761	0.761	49.51	49.51	365.34	365.34
	RF	0.751	0.752	50.47	50.45	950.49	931.58
	PointNet	0.722	0.766	53.40	48.99	2039.97	997.48
	KPConv	0.796	0.806	45.72	44.60	268.63	204.02
	MSENet14	0.819	0.823	43.00	42.58	230.36	102.16
	MSENet50	0.815	0.821	43.59	42.78	127.33	99.43
volume	linear	0.760	0.760	93.52	93.52	172.91	172.91
	power	0.763	0.763	92.82	92.82	223.64	223.64
	RF	0.755	0.756	94.38	94.34	217.50	216.40
	PointNet	0.727	0.772	99.64	91.09	470.42	262.44
	KPConv	0.788	0.801	87.95	85.16	86.47	73.05
	MSENet14	0.813	0.818	82.55	81.45	70.05	65.69
	MSENet50	0.810	0.816	83.16	81.84	69.15	68.99

$$b^* = \frac{\sum_{i=1}^N (y_i - \mathbf{a}^T h_\theta(\mathbf{x}_i))}{N} . \quad (6)$$

This bias correction can also be applied to other non-linear models h_θ (e.g., h_θ could be a random forest); h_θ can be wrapped according to (5) with scalar $a = 1$ and b set to b^* computed by (6).

3 Results

We conducted a detailed comparison of all methods for predicting AGB (and thereby above-ground carbon stocks) and wood volume. We used the root-mean-square-error (RMSE), the coefficient of determination R^2 , and the mean absolute percentage error (MAPE) as evaluation metrics, in accordance with the related literature. The prediction bias parameter was calibrated on the training and validation set for all non-linear methods (all except linear regression) as described in Section 2.4 [Igel and Oehmcke, 2022].

An overview of the results is given in Tab. 2 showing the R^2 , RMSE, and MAPE for the different algorithms on the test set, which was not used for model development. Overall, the MSENet14 model achieved the best results with an R^2 of 0.823 for biomass (and carbon stocks) and an R^2 of 0.818 for wood volume. The corresponding RMSEs were 42.58 Mg ha⁻¹ and 81.45 m³ ha⁻¹, respectively.

The RF performed the worst. The better performance of the linear regression with an R^2 of 0.757 for biomass and 0.760 for wood volume, indicates that the calculated features are to a certain extent linearly correlated with the target

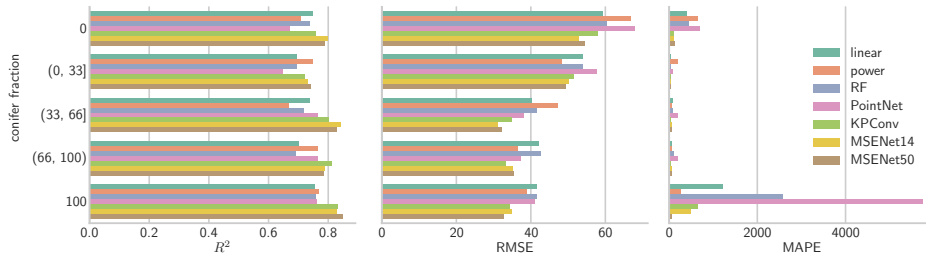


Figure 6: Errors for different fractions of conifer and broadleaf trees for biomass on the test set. The columns show R^2 (higher is better), RMSE (lower is better), and MAPE (lower is better). The corresponding figure for wood volume is qualitatively the same.

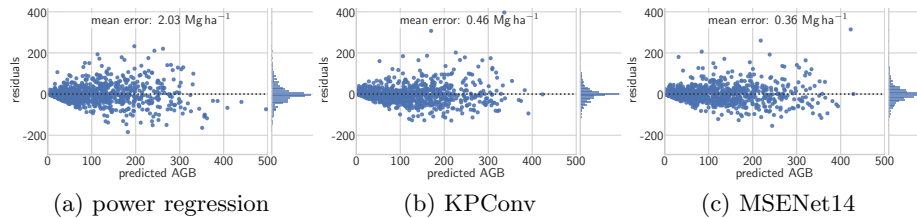


Figure 7: Biomass residual (left side) and error distribution (right side) plots of the test performance for power regression, KPConv, and MSENNet14. The mean error is given as well to quantify the observed bias.

variables. The power regression model based on [Magnussen et al. \[2018\]](#) reached R^2 values of 0.761 and 0.763 for biomass and tree volume, respectively, that is, the deep learning approach clearly improved over the state-of-the-art methods. All more recent point cloud based methods outperformed the models based on the precomputed features, justifying that the networks indeed utilized additional information from the point clouds. The MAPE, which was not an optimization criterion, showed the largest differences between the methods, which are mainly attributed to errors related to small target values.

The national forest inventory data offers information about the fraction of conifer and broadleaf for each site, which we used to analyze the performance at different fractions in Fig. 6. Interestingly, KPConv performed better than the Minkowski models for conifer fraction interval (66, 100] and nearly equally good at 100. Again, the high MAPE for the baseline methods that rely on the precomputed features and PointNet was noticeable, in particular when mono cultures were analyzed. In general, mono cultures turned out to be more difficult than mixed forests w.r.t. MAPE but not w.r.t. RMSE and R^2 (e.g., forests with conifer trees only exhibited the lowest RMSE and R^2).

The spread of errors increased with magnitude of the target variables as seen in Fig. 7 for the power, KPConv, and MSENNet14 model. While low values were more often overestimated, high values tended to be underestimated. Comparing the distribution of errors as well as the mean error of the assessed models, one can see that the KPConv and Minkowski models had a generally lower spread of errors than the power model. See Fig. 11 and 12 in the appendix for the remaining plots.

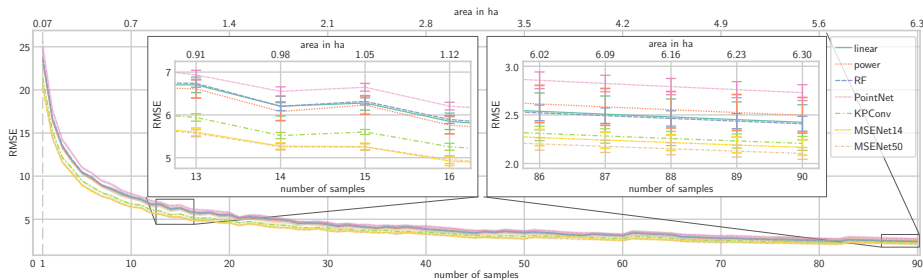


Figure 8: Experiment showing that errors cancel out if the area is increased. The ordinate shows the carbon stock RMSE in Mg C ha^{-1} . The abscissa indicates the number of randomly sampled subplots that are combined. Each subplot has a size of ≈ 0.07 ha, so 14 samples correspond to little less than 1 ha. The error bars indicate the standard error over 10 different random combinations of subplots for each model repetition.

It has been found that the errors of ALS-based carbon stock estimates decrease when increasing the size of the observed area (e.g., aggregating over a larger area decreases the error [Asner et al., 2010, Mascaro et al., 2011, Dalponte and Coomes, 2016, Ferraz et al., 2016]). To demonstrate this, we calculated the RMSE for each model over the same randomly chosen combination of subplots (Fig. 8). We repeated that process 10 times with different random combinations for each model repetition. The predictions for the combined plots were added and compared to the aggregated measurements. We consider the carbon stock RMSE in Mg C ha^{-1} to allow for easier comparison with published results. The RMSE reduces quickly for all models and the ranking of models remains the same.

4 Discussion

The results give clear evidence that the deep learning approaches KPConv and MSENNet are preferable to the methods working on point cloud statistics. As the time to apply and train MSENNet is drastically shorter (see Tab. 1) and the results were marginally better, we regard MSENNet as the method of choice. We assume that the subpar performance of PointNet is due to the missing local context processing in the algorithm, which seems to be required for forest scenes.

4.1 Quantitative comparison to other studies

Caution is warranted when comparing our prediction accuracy with that of other studies. Reported errors of ALS-based prediction models for AGB range from 17 to 40 Mg ha^{-1} in the tropics [Asner et al., 2011], and this error is comparable to estimates reported in other regions [Lefsky et al., 2002] as well as previous studies with the Danish NFI [Nord-Larsen and Schumacher, 2012]. Reassuringly, we achieve error rates at the lower end of this spectrum. It is important to emphasize, however, that it is not uncommon that the indicators documented in these studies measure the error on a training data set as a goodness of fit index (e.g., in the study by Lefsky et al., 1999 the R^2 for AGB drops from 80 %

down to 33% when the model is applied to a different data set). Similarly but not as severe, earlier studies of the Danish NFI with fewer data also reported a 0.6% increase in RMSE when using hold-out sets [Nord-Larsen and Schumacher, 2012]. Conversely, the training errors of our models are similar to the test set results in Tab. 2 (see Tab. 3 in the supplementary material), indicating that the models are not overfitted.

The error of the overall carbon stock prediction has been shown to decrease with increasing area, which is explained by error cancellation [Asner et al., 2010, Mascaro et al., 2011, Dalponte and Coomes, 2016, Ferraz et al., 2016, Magnussen et al., 2018]. This is an important property when it comes to country-wide quantification of carbon. For example, in the study by Mascaro et al. [2011], the RMSE of the estimated carbon stocks decreased from 63.2 to 11.1 and then to 6.5 Mg C ha⁻¹ when the observed area was increased from 0.04 to 1 and then to 6.25 ha. Our study areas are of size $a = 15^2 \cdot \pi \cdot 10^{-4}$ ha ≈ 0.07 ha. The residuals in Fig. 7 indeed suggest that our errors average out if several subplots are combined. This is confirmed by the results shown in Fig. 8. For aggregated areas of approximately 1 ha (with 14 samples it is 0.98 ha) and 6.25 ha (with 89 samples it is 6.23 ha), the RMSE for the MSENNet14 model was 5.28 (SE 0.09) and 2.19 (SE 0.09), respectively. Even though the errors cancel out, a good high-resolution performance seems to translate to a better aggregated performance.

4.2 Applicability and map generation

The results are evaluated on an previously unseen and non-overlapping test set, meaning that the model should exhibit a similar performance on other arbitrarily chosen forest subplots from the study area (e.g., Denmark). For new study areas that are dissimilar to ours (e.g., different climate zone, tree species, or topographical features), reevaluation and potential fine-tuning of the models would be needed. However, since little preprocessing is required, this verification and adjustment step is comparatively minor.

Our method allows for dense, non-interpolated biomass mappings with unprecedented accuracy at large scale at a resolution below 30 m. An exemplary biomass map is demonstrated in Fig. 9. The figure shows the results of the MSENNet50 model applied to a randomly selected 1 km area in Denmark without any additional preprocessing. The results are convincing, as areas with no points above ground are predicted to have no biomass, and areas with many trees have high biomass. Thus, our method enables highly accurate analyses of the AGB development in Denmark by comparing AGB maps from different years.

5 Conclusions

Precise quantification of the spatial distribution of forest biomass and carbon content is a valuable tool to understand the processes driving af-, re-, and deforestation, and the variations in carbon cycle from the ecosystem to the regional and global scale [Zolkos et al., 2013].

This study brings forward deep learning systems for predicting above-ground biomass, wood volume, and carbon stocks in forests efficiently and directly from airborne LiDAR point clouds. Three conceptually different neural network ar-

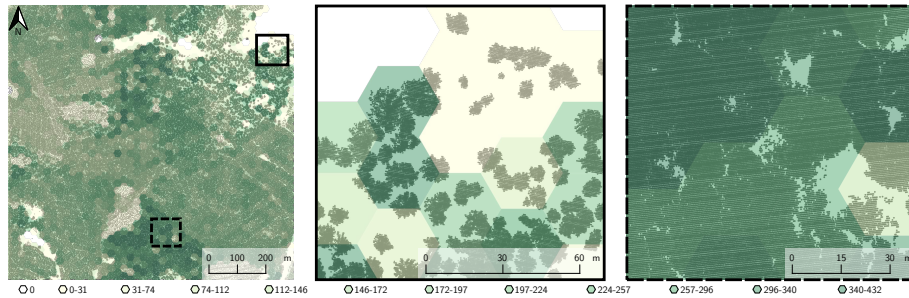


Figure 9: Exemplary map showing predictions at different zoom levels. Points of the point cloud colored grey (only ≈ 1 m above the ground) and overlaid with the estimated biomass in Mg ha^{-1} , where a deeper green indicates more biomass.

architectures for classification (i.e., PointNet, KPConv, and Minkowski CNNs) were modified to perform regression, and were evaluated using a unique data set combining field measurements and LiDAR data.

Our adaptation of Minkowski CNNs outperformed the other deep learning approaches as well as the baseline methods. Specifically, the coefficient of determination R^2 for above-ground biomass and stored carbon exceeded 0.82 at 0.07 ha on a test set, which was not considered in the modelling process. The main advantage of the method proposed is the efficient implementation of 3D convolutions for sparse data, as it relies on the same operations that CNNs use for standard image processing.

The assessed deep learning models achieved high accuracies, leading to a considerably better performance in predicting AGB of forest areas, compared to the state-of-the-art approach operating on basic statistics of the point clouds. Our approach simplifies the production of AGB and carbon content maps at high resolution. It does neither require digital elevation models (e.g., DTMs or canopy height models) nor forest canopies with structural heterogeneity.

These encouraging results may be the first step towards a paradigm shift in utilizing LiDAR data for accurate quantification and analysis of forest carbon dynamics, which is a key component for achieving the United Nations Strategic Plan for Forests under the Paris agreement and the Sustainable Development Goals (SDGs) [United Nations Department of Economic and Social Affairs, 2021, 2017] in accordance with the IPCC 2018 [Masson-Delmotte et al., 2019].

Acknowledgement

This work was supported by the research grant DeReEco (34306) from Villum Foundations, the Independent Research Fund Denmark through the grant *Monitoring Changes in Big Satellite Data via Massively-Parallel Artificial Intelligence* (9131-00110B), a Villum Experiment grant by the Velux Foundations (MapCland project, project number: 00028314), the DeepCrop project (UCPH Strategic plan 2023 Data+ Pool), and the Pioneer Centre for AI, DNRF grant number P1.

References

- Gregory P Asner and Joseph Mascaro. Mapping tropical forest carbon: Calibrating plot estimates to a simple lidar metric. *Remote Sensing of Environment*, 140:614–624, 2014.
- Gregory P Asner, George VN Powell, Joseph Mascaro, David E Knapp, John K Clark, James Jacobson, Ty Kennedy-Bowdoin, Aravindh Balaji, Guayana Paez-Acosta, Eloy Victoria, et al. High-resolution forest carbon stocks and emissions in the Amazon. *Proceedings of the National Academy of Sciences*, 107(38):16738–16742, 2010.
- Gregory P. Asner, R. Flint Hughes, Joseph Mascaro, Amanda L. Uowolo, David E. Knapp, James Jacobson, Ty Kennedy-Bowdoin, and John K. Clark. High-resolution carbon mapping on the million-hectare island of Hawaii. *Frontiers in Ecology and the Environment*, 9(8):434–439, 2011.
- Marc Bouvier, Sylvie Durrieu, Richard A Fournier, and Jean-Pierre Renaud. Generalizing predictive models of forest inventory attributes using an area-based approach with airborne lidar data. *Remote Sensing of Environment*, 156:322–334, 2015.
- Leo Breiman. Random forests. *Machine Learning*, 45(1):5–32, 2001.
- CARTO. map style. <https://carto.com/>, 2023.
- Angel X. Chang, Thomas A. Funkhouser, Leonidas J. Guibas, Pat Hanrahan, Qi-Xing Huang, Zimo Li, Silvio Savarese, Manolis Savva, Shuran Song, Hao Su, Jianxiong Xiao, Li Yi, and Fisher Yu. Shapenet: An information-rich 3D model repository. *CoRR*, abs/1512.03012, 2015.
- Thomas Chaton, Chaulet Nicolas, Sofiane Horache, and Loic Landrieu. Torch-Points3D: A modular multi-task framework for reproducible deep learning on 3D point clouds. In *3D Vision (3DV)*, pages 1–10. IEEE, 2020.
- Christopher Choy, JunYoung Gwak, and Silvio Savarese. 4D spatio-temporal convnets: Minkowski convolutional neural networks. In *IEEE / CVF Computer Vision and Pattern Recognition Conference (CVPR)*, pages 3075–3084, 2019.
- Djork-Arné Clevert, Thomas Unterthiner, and Sepp Hochreiter. Fast and accurate deep network learning by exponential linear units (ELUs). In *International Conference on Learning Representation (ICLR)*, 2016.
- Susan C Cook-Patton, Sara M Leavitt, David Gibbs, Nancy L Harris, Kristine Lister, Kristina J Anderson-Teixeira, Russell D Briggs, Robin L Chazdon, Thomas W Crowther, Peter W Ellis, et al. Mapping carbon accumulation potential from global natural forest regrowth. *Nature*, 585(7826):545–550, 2020.
- D. Barry Coyle, Paul R. Stysley, Furqan L. Chirag, Erich Frese, and Demetrios Poullos. The global ecosystem dynamics investigation (GEDI) LiDAR laser transmitter. In *Infrared Remote Sensing and Instrumentation XXVII*, volume 11128, pages 112–125. Int. Society for Optics and Photonics, 2019.

- Michele Dalponte and David A Coomes. Tree-centric mapping of forest carbon density from airborne laser scanning and hyperspectral data. *Methods in ecology and evolution*, 7(10):1236–1245, 2016.
- Marcus VN d’Oliveira, Stephen E Reutebuch, Robert J McGaughey, and Hans-Erik Andersen. Estimating forest biomass and identifying low-intensity logging areas using airborne scanning lidar in antimary state forest, acre state, western brazilian amazon. *Remote Sensing of Environment*, 124:479–491, 2012.
- Karl-Heinz Erb, Thomas Kastner, Christoph Plutzer, Anna Liza S Bais, Nuno Carvalhais, Tamara Fetzel, Simone Gingrich, Helmut Haberl, Christian Lauk, Maria Niedertscheider, Julia Pongratz, Martin Thurner, and Sebastiaan Luysaert. Unexpectedly large impact of forest management and grazing on global vegetation biomass. *Nature*, 553(7686):73–76, 2018.
- FAO and UNEP. The state of the world’s forests 2020. forests, biodiversity and people, 2020.
- FE Fassnacht, F Hartig, H Latifi, C Berger, J Hernández, P Corvalán, and B Koch. Importance of sample size, data type and prediction method for remote sensing-based estimations of aboveground forest biomass. *Remote Sensing of Environment*, 154:102–114, 2014.
- António Ferraz, Sassan Saatchi, Clément Mallet, and Victoria Meyer. Lidar detection of individual tree size in tropical forests. *Remote Sensing of Environment*, 183:318–333, 2016.
- Ahmet Firintepe, Carolin Vey, Stylianos Asteriadis, Alain Pagani, and Didier Stricker. From IR images to point clouds to pose: Point cloud-based AR glasses pose estimation. *Journal of Imaging*, 7(5), 2021. ISSN 2313-433X.
- Liuhaio Ge, Zhou Ren, and Junsong Yuan. Point-to-point regression PointNet for 3D hand pose estimation. In *European Conference on Computer Vision (ECCV)*, pages 475–491, 2018.
- Ross Girshick. Fast R-CNN. In *International Conference on Computer Vision (ICCV)*, pages 1440–1448, 2015.
- Scott Goetz and Ralph Dubayah. Advances in remote sensing technology and implications for measuring and monitoring forest carbon stocks and change. *Carbon Management*, 2(3):231–244, 2011.
- Nicholas R Goodwin, Nicholas C Coops, and Darius S Culvenor. Assessment of forest structure with airborne lidar and the effects of platform altitude. *Remote Sensing of Environment*, 103(2):140–152, 2006.
- Ben Graham. Sparse 3D convolutional neural networks. In *BMVC*, pages 150.1–150.9, 2015.
- Benjamin Graham, Martin Engelcke, and Laurens Van Der Maaten. 3D semantic segmentation with submanifold sparse convolutional networks. In *IEEE / CVF Computer Vision and Pattern Recognition Conference (CVPR)*, pages 9224–9232, 2018.

- Bronson W. Griscom, Justin Adams, Peter W. Ellis, Richard A. Houghton, Guy Lomax, Daniela A. Miteva, William H. Schlesinger, David Shoch, Juha V. Siikamäki, Pete Smith, Peter Woodbury, Chris Zganjar, Allen Blackman, João Campari, Richard T. Conant, Christopher Delgado, Patricia Elias, Trisha Gopalakrishna, Marisa R. Hamsik, Mario Herrero, Joseph Kiesecker, Emily Landis, Lars Laestadius, Sara M. Leavitt, Susan Minnemeyer, Stephen Polasky, Peter Potapov, Francis E. Putz, Jonathan Sanderman, Marcel Silvius, Eva Wollenberg, and Joseph Fargione. Natural climate solutions. *Proceedings of the National Academy of Sciences*, 114(44):11645–11650, 2017.
- Yulan Guo, Hanyun Wang, Qingyong Hu, Hao Liu, Li Liu, and Mohammed Bennamoun. Deep learning for 3d point clouds: A survey. *transactions on pattern analysis and machine intelligence (PAMI)*, 43(12):4338–4364, 2020. doi: 10.1109/TPAMI.2020.3005434.
- Timo Hackel, N. Savinov, L. Ladicky, Jan D. Wegner, K. Schindler, and M. Pollefeys. SEMANTIC3D.NET: A new large-scale point cloud classification benchmark. In *ISPRS Annals of the Photogrammetry, Remote Sensing and Spatial Information Sciences*, volume IV-1-W1, pages 91–98, 2017.
- Steven Hancock, John Armston, Michelle Hofton, Xiaoli Sun, Hao Tang, Laura I Duncanson, James R Kellner, and Ralph Dubayah. The gedi simulator: A large-footprint waveform lidar simulator for calibration and validation of spaceborne missions. *Earth and Space Science*, 6(2):294–310, 2019.
- Nancy L Harris, Sandra Brown, Stephen C Hagen, Sassan S Saatchi, Silvia Petrova, William Salas, Matthew C Hansen, Peter V Potapov, and Alexander Lotsch. Baseline map of carbon emissions from deforestation in tropical regions. *Science*, 336(6088):1573–1576, 2012.
- Nancy L Harris, David A Gibbs, Alessandro Baccini, Richard A Birdsey, Sytze De Bruin, Mary Farina, Lola Fatoyinbo, Matthew C Hansen, Martin Herold, Richard A Houghton, et al. Global maps of twenty-first century forest carbon fluxes. *Nature Climate Change*, 11(3):234–240, 2021.
- Jie Hu, Li Shen, and Gang Sun. Squeeze-and-excitation networks. In *IEEE / CVF Computer Vision and Pattern Recognition Conference (CVPR)*, pages 7132–7141, 2018.
- Christian Igel and Stefan Oehmcke. Remember to correct the bias when using deep learning for regression! *Künstliche Intelligenz*, 2022. (in press).
- Vivian Kvist Johannsen. *A growth model for oak in Denmark*. PhD thesis, Royal Veterinary and Agricultural University, Copenhagen, Denmark, 1999.
- Leslie Kish. Space/time variations and rolling samples. *Journal of Official Statistics*, 14(1):31, 1998.
- Nikolai Knapp, Rico Fischer, and Andreas Huth. Linking lidar and forest modeling to assess biomass estimation across scales and disturbance states. *Remote Sensing of Environment*, 205:199–209, 2018.

- Nikolai Knapp, Rico Fischer, Victor Cazcarra-Bes, and Andreas Huth. Structure metrics to generalize biomass estimation from lidar across forest types from different continents. *Remote Sensing of Environment*, 237:111597, 2020.
- Nico Lang, Konrad Schindler, and Jan Dirk Wegner. High carbon stock mapping at large scale with optical satellite imagery and spaceborne LIDAR. *CoRR*, 2021.
- Nico Lang, Nikolai Kalischek, John Armston, Konrad Schindler, Ralph Dubayah, and Jan Dirk Wegner. Global canopy height regression and uncertainty estimation from GEDI lidar waveforms with deep ensembles. *Remote Sensing of Environment*, 268:112760, 2022.
- Yann LeCun, Yoshua Bengio, and Geoffrey Hinton. Deep learning. *Nature*, 521(7553):436–444, 2015.
- Michael A. Lefsky, D. Harding, W. B. Cohen, G Parker, and H. H. Shugart. Surface lidar remote sensing of basal area and biomass in deciduous forests of eastern Maryland, USA. *Remote Sensing of Environment*, 67(1):83–98, 1999. ISSN 0034-4257.
- Michael A. Lefsky, Warren B. Cohen, David J. Harding, Geoffrey G. Parker, Steven A. Acker, and S. Thomas Gower. Lidar remote sensing of above-ground biomass in three biomes. *Global Ecology and Biogeography*, 11(5):393–399, 2002.
- Simon L Lewis, Charlotte E Wheeler, Edward TA Mitchard, and Alexander Koch. Regenerate natural forests to store carbon. *Nature*, 568(7750):25–28, 2019.
- Yingchang Li, Mingyang Li, Chao Li, and Zhenzhen Liu. Forest aboveground biomass estimation using landsat 8 and sentinel-1a data with machine learning algorithms. *Scientific Reports*, 10(1):1–12, 2020.
- Ilya Loshchilov and Frank Hutter. SGDR: stochastic gradient descent with warm restarts. In *International Conference on Learning Representation (ICLR)*. OpenReview.net, 2017.
- Ilya Loshchilov and Frank Hutter. Decoupled weight decay regularization. In *International Conference on Learning Representation (ICLR)*. OpenReview.net, 2019.
- Steen Magnussen, E Næsset, T Gobakken, and G Frazer. A fine-scale model for area-based predictions of tree-size-related attributes derived from lidar canopy heights. *Scandinavian Journal of Forest Research*, 27(3):312–322, 2012.
- Steen Magnussen, Thomas Nord-Larsen, and Torben Riis-Nielsen. Lidar supported estimators of wood volume and aboveground biomass from the Danish national forest inventory (2012–2016). *Remote Sensing of Environment*, 211:146–153, 2018.
- Joseph Mascaro, Matteo Detto, Gregory P. Asner, and Helene C. Muller-Landau. Evaluating uncertainty in mapping forest carbon with airborne LIDAR. *Remote Sensing of Environment*, 115(12):3770–3774, 2011.

- V. Masson-Delmotte, P. Zhai, H.-O. Pörtner, D. Roberts, J. Skea, P.R. Shukla, A. Pirani, W. Moufouma-Okia, C. Péan, R. Pidcock, S. Connors, J. B. R. Matthews, Y. Chen, X. Zhou, M.I. Gomis, E. Lonnoy, T. Maycock, M. Tignor, and T. Waterfield, editors. *IPCC, 2018: Global Warming of 1.5°C. An IPCC Special Report on the impacts of global warming of 1.5°C above pre-industrial levels and related global greenhouse gas emission pathways, in the context of strengthening the global response to the threat of climate change, sustainable development, and efforts to eradicate poverty*. Cambridge University Press, 2019.
- Trent L. McDonald. Review of environmental monitoring methods: survey designs. *Environmental Monitoring and Assessment*, 85(3):277–292, 2003.
- Stéphane Mermoz, Maxime Réjou-Méchain, Ludovic Villard, Thuy Le Toan, Vivien Rossi, and Sylvie Gourlet-Fleury. Decrease of l-band sar backscatter with biomass of dense forests. *Remote Sensing of Environment*, 159:307–317, 2015.
- Edward T. A. Mitchard, Sassan S. Saatchi, Lee J. T. White, Katharine Anne Abernethy, Kathryn Jane Jeffery, Simon L. Lewis, Murray Collins, Michael A. Lefsky, Miguel E. Leal, Iain H. Woodhouse, and Patrick Meir. Mapping tropical forest biomass with radar and spaceborne LiDAR in Lopé National Park, Gabon: overcoming problems of high biomass and persistent cloud. *Biogeosciences*, 9(1):179–191, 2012.
- Erik Næsset. Effects of different sensors, flying altitudes, and pulse repetition frequencies on forest canopy metrics and biophysical stand properties derived from small-footprint airborne laser data. *Remote Sensing of Environment*, 113(1):148–159, 2009.
- Manfred Näslund. Skogsförsöksanstaltens gallringsförsök i tallskog. *Meddelanden från Statens skogsförsöksanstalt*, 29:1–169, 1936.
- Thomas Nord-Larsen and Vivian Kvist Johannsen. Danish national forest inventory: Design and calculations. *IGN Report, Department of Geosciences and Natural Resource Management, University of Copenhagen*, 2016.
- Thomas Nord-Larsen and Johannes Schumacher. Estimation of forest resources from a country wide laser scanning survey and national forest inventory data. *Remote Sensing of Environment*, 119:148–157, 2012. ISSN 0034-4257. doi: <https://doi.org/10.1016/j.rse.2011.12.022>.
- Thomas Nord-Larsen, Henrik Meilby, and Jens Peter Skovsgaard. Simultaneous estimation of biomass models for 13 tree species: effects of compatible additive requirements. *Canadian J. of Forest Research*, 47(6):765–776, 2017a.
- Thomas Nord-Larsen, Torben Riis-Nielsen, and Mathias Bo Ottosen. Forest resource map of Denmark: Mapping of Danish forest resource using ALS from 2014–2015. *IGN Report, Department of Geosciences and Natural Resource Management, University of Copenhagen*, 2017b.
- Stefan Oehmcke, Lei Li, Jaime Revenga, Thomas Nord-Larsen, Katerina Trepekli, Fabian Gieseke, and Christian Igel. Deep learning based 3D point

- cloud regression for estimating forest biomass. In *International Conference on Advances in Geographic Information Systems (SIGSPATIAL)*. ACM, 2022.
- Anthony R. Olsen, Joseph Sedransk, Don Edwards, Carol A. Gotway, Walter Liggett, Stephen Rathbun, Kenneth H. Reckhow, and Linda J. Yyoung. Statistical issues for monitoring ecological and natural resources in the united states. *Environmental Monitoring and Assessment*, 54(1):1–45, 1999.
- OpenMapTiles. base map. <http://openmaptiles.org/>, 2023.
- Liyuan Pan, Liu Liu, Anthony G Condon, Gonzalo M Estavillo, Robert A Coe, Geoff Bull, Eric A Stone, Lars Petersson, and Vivien Rolland. Biomass prediction with 3d point clouds from LiDAR. In *Winter Conference on Applications of Computer Vision (WACV)*, pages 1330–1340, 2022.
- Yude Pan, Richard A Birdsey, Oliver L Phillips, and Robert B Jackson. The structure, distribution, and biomass of the world’s forests. *Annual Review of Ecology, Evolution, and Systematics*, 44:593–622, 2013.
- Adam Paszke, Sam Gross, Francisco Massa, Adam Lerer, James Bradbury, Gregory Chanan, Trevor Killeen, Zeming Lin, Natalia Gimelshein, Luca Antiga, et al. Pytorch: An imperative style, high-performance deep learning library. *NeurIPS*, 32:8026–8037, 2019.
- Fabian Pedregosa, Gaël Varoquaux, Alexandre Gramfort, Vincent Michel, Bertrand Thirion, Olivier Grisel, Mathieu Blondel, Peter Prettenhofer, Ron Weiss, Vincent Dubourg, Jake Vanderplas, Alexandre Passos, and David Cournapeau. Scikit-learn: Machine learning in Python. *Journal of Machine Learning Research*, 12:2825–2830, 2011.
- Charles R. Qi, Hao Su, Kaichun Mo, and Leonidas J. Guibas. PointNet: Deep learning on point sets for 3D classification and segmentation. In *IEEE / CVF Computer Vision and Pattern Recognition Conference (CVPR)*, pages 652–660, 2017.
- Charles R. Qi, Or Litany, Kaiming He, and Leonidas J. Guibas. Deep hough voting for 3d object detection in point clouds. In *International Conference on Computer Vision (ICCV)*, pages 9276–9285. IEEE, 2019.
- Daniela Requena Suarez, Danaë MA Rozendaal, Veronique De Sy, Oliver L Phillips, Esteban Alvarez-Dávila, Kristina Anderson-Teixeira, Alejandro Araujo-Murakami, Luzmila Arroyo, Timothy R Baker, Frans Bongers, et al. Estimating aboveground net biomass change for tropical and subtropical forests: Refinement of IPCC default rates using forest plot data. *Global change biology*, 25(11):3609–3624, 2019.
- Priyadarshi R Shukla, J Skeg, E Calvo Buendia, Valérie Masson-Delmotte, H-O Pörtner, DC Roberts, Panmao Zhai, Raphael Slade, Sarah Connors, R. van Diemen, M. Ferrat, E. Haughey, S. Luz, S. Neogi, M. Pathak, J. Petzold, J. Portugal Pereira, P. Vyas, E. Huntley, K. Kissick, M. Belkacemi, and J. Malley, editors. *IPCC, 2019: Climate Change and Land: an IPCC special report on climate change, desertification, land degradation, sustainable land management, food security, and greenhouse gas fluxes in terrestrial ecosystems*. Cambridge University Press, 2019.

- Suman Sinha, Chockalingam Jeganathan, Laxmi Kant Sharma, and Mahendra Singh Nathawat. A review of radar remote sensing for biomass estimation. *Int. Journal of Environmental Science and Technology*, 12(5):1779–1792, 2015.
- Branislav Sloboda, Dieter Gaffrey, and Naoto Matsumura. Regionale und lokale Systeme von Höhenkurven für gleichaltrige Waldbestände. *Allgemeine Forst- und Jagdzeitung*, 164(12):225–228, 1993.
- Scott C Stark, Veronika Leitold, Jin L Wu, Maria O Hunter, Carolina V de Castilho, Flávia RC Costa, Sean M McMahon, Geoffrey G Parker, Mônica Takako Shimabukuro, Michael A Lefsky, et al. Amazon forest carbon dynamics predicted by profiles of canopy leaf area and light environment. *Ecology Letters*, 15(12):1406–1414, 2012.
- Hugues Thomas, Charles R. Qi, Jean-Emmanuel Deschaud, Beatriz Marcotegui, François Goulette, and Leonidas J. Guibas. KPConv: Flexible and deformable convolution for point clouds. *International Conference on Computer Vision (ICCV)*, pages 6411–6420, 2019.
- Robert Treuhaft, Fabio Gonçalves, João Roberto dos Santos, Michael Keller, Michael Palace, Søren N Madsen, Franklin Sullivan, and Paulo MLA Graça. Tropical-forest biomass estimation at x-band from the spaceborne tandem-x interferometer. *IEEE Geoscience and Remote Sensing Letters*, 12(2):239–243, 2014.
- Francesco N Tubiello, Giulia Conchedda, Nathan Wanner, Sandro Federici, Simone Rossi, and Giacomo Grassi. Carbon emissions and removals from forests: new estimates, 1990–2020. *Earth System Science Data*, 13(4):1681–1691, 2021.
- United Nations / Framework Convention on Climate Change. Paris agreement, 2015. Report of the Conference of the Parties to the United Nations Framework Convention on Climate Change (21st Session, 2015: Paris).
- United Nations Department of Economic and Social Affairs. The sustainable development goals report, 2017.
- United Nations Department of Economic and Social Affairs. The global forest goals report 2021, 2021.
- Zhirong Wu, Shuran Song, Aditya Khosla, Fisher Yu, Linguang Zhang, Xiaoou Tang, and Jianxiong Xiao. 3d shapenets: A deep representation for volumetric shapes. In *IEEE / CVF Computer Vision and Pattern Recognition Conference (CVPR)*, pages 1912–1920. IEEE Computer Society, 2015.
- Linjing Zhang, Zhenfeng Shao, Jianchen Liu, and Qimin Cheng. Deep learning based retrieval of forest aboveground biomass from combined LiDAR and landsat 8 data. *Remote Sensing*, 11(12):1459, 2019.
- Wenyang Zhang, Qiwei Yao, Howell Tong, and Nils Chr. Stenseth. Smoothing for spatiotemporal models and its application to modeling Muskrat-Mink interaction. *Biometrics*, 59(4):813–821, 2003.

Yin Zhou and Oncel Tuzel. Voxelnet: End-to-end learning for point cloud based 3d object detection. In *IEEE / CVF Computer Vision and Pattern Recognition Conference (CVPR)*, pages 4490–4499, 2018.

Scott G. Zolkos, Scott J. Goetz, and Ralph Dubayah. A meta-analysis of terrestrial aboveground biomass estimation using lidar remote sensing. *Remote Sensing of Environment*, 128:289–298, 2013.

Table 3: Comparison of methods showing the R^2 score, RMSE, and MAPE on the training set. The models with best validation set performances were chosen. The R^2 and MAPE for biomass are the same as for carbon stocks. Note that we excluded 0 biomass measurements from MAPE to avoid numerical issues. Best results are highlighted.

target	model	R^2		RMSE		MAPE	
		med.	max	med.	min	med.	min
AGB	linear	0.712	0.712	55.47	55.47	770.03	770.03
	power	0.700	0.700	56.63	56.63	690.59	690.59
	RF	0.759	0.760	50.75	50.73	553.61	548.55
	PointNet	0.684	0.706	58.16	56.13	2146.63	1273.65
	KPConv	0.795	0.799	46.84	46.37	267.56	129.17
	MSENet14	0.786	0.794	47.81	46.91	318.26	259.58
	MSENet50	0.791	0.800	47.32	46.22	250.04	184.65
volume	linear	0.716	0.716	103.51	103.51	188.70	188.70
	power	0.703	0.703	105.83	105.83	197.08	197.08
	RF	0.765	0.765	94.15	94.11	157.32	156.09
	PointNet	0.694	0.714	107.39	103.92	431.84	283.08
	KPConv	0.792	0.798	88.58	87.38	91.97	68.84
	MSENet14	0.784	0.792	90.27	88.54	96.16	81.57
	MSENet50	0.794	0.801	88.19	86.57	87.61	85.31

A Additional Results

Tab. 3 and Tab. 4 presents the results on the training and validation set, respectively. Note that the models using extracted features (linear regression, power regression, and RF) were trained on the union of training and validation set, while our point cloud regression models were not. Still, the more recent models directly working on the point cloud data consistently produced better results. Fig. 11 and 12 illustrate residual plots and error distribution of biomass and wood volume, respectively, which completes Fig. 7.

In Fig. 13 we show more subplots with particularly low or high values for above-ground biomass. For example, the first two subplots have low AGB with 1.79 and 1.89 Mg ha^{-1} , which is reflected by the sparse vegetation in the point cloud. This is difficult to capture with commonly used statistics derived from point cloud data, and therefore models based on these features (e.g., RF, lin., and power model) overestimated. Interestingly, PointNet also overestimate values due to the employed global aggregation without intermediate downsampling steps (similar to global feature extraction). The third example in Fig. 13 exhibits a high AGB value with $417.60 \text{ Mg ha}^{-1}$ and the point cloud shows a densely populated and natural broadleaf forest. Again, this is difficult to estimate since the derived statistics do not offer information about individual biomass contributions and thus most methods underestimate them. The fourth subplots biomass is $245.89 \text{ Mg ha}^{-1}$ from a conifer forest and the predictions align well with the target. We also give a visualization of the plots and subplots in Fig. 14 (as described in Sec. 2.1).

Table 4: Comparison of methods showing the R^2 score, RMSE, and MAPE on the validation set. The R^2 and MAPE for biomass are the same as for carbon stocks. Note that we excluded 0 biomass measurements from MAPE to avoid numerical issues. Best results are highlighted. Note that the deep learning models did not train on this data directly but the feature extraction methods did.

target	model	R^2		RMSE		MAPE	
		med.	max	med.	min	med.	min
AGB	linear	0.736	0.736	54.37	54.37	388.13	388.13
	power	0.739	0.739	53.99	53.99	384.63	384.63
	RF	0.775	0.775	50.16	50.12	398.48	375.35
	PointNet	0.685	0.728	59.32	55.21	1811.21	1303.69
	KPConv	0.773	0.775	50.37	50.19	176.69	144.17
	MSENet14	0.796	0.798	47.77	47.49	207.74	92.94
	MSENet50	0.805	0.810	46.70	46.08	71.72	61.81
volume	linear	0.764	0.764	95.05	95.05	114.59	114.59
	power	0.766	0.766	94.61	94.61	118.03	118.03
	RF	0.800	0.801	87.45	87.40	111.73	109.71
	PointNet	0.719	0.760	103.81	95.94	322.45	205.49
	KPConv	0.794	0.800	88.87	87.61	72.38	65.82
	MSENet14	0.814	0.816	84.44	83.95	69.24	60.66
	MSENet50	0.824	0.826	82.20	81.53	61.76	61.22

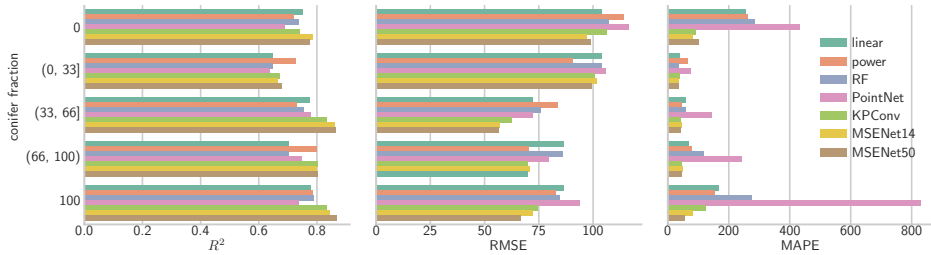


Figure 10: Errors for different fractions of conifer and broadleaf trees for wood volume on the test set. The columns show R^2 (higher is better), RMSE (lower is better), and MAPE (lower is better).

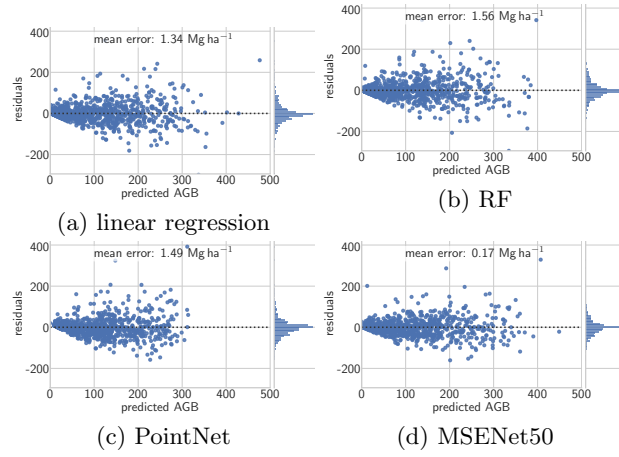


Figure 11: Biomass residual (left side) and error distribution (right side) plots of the test performance.

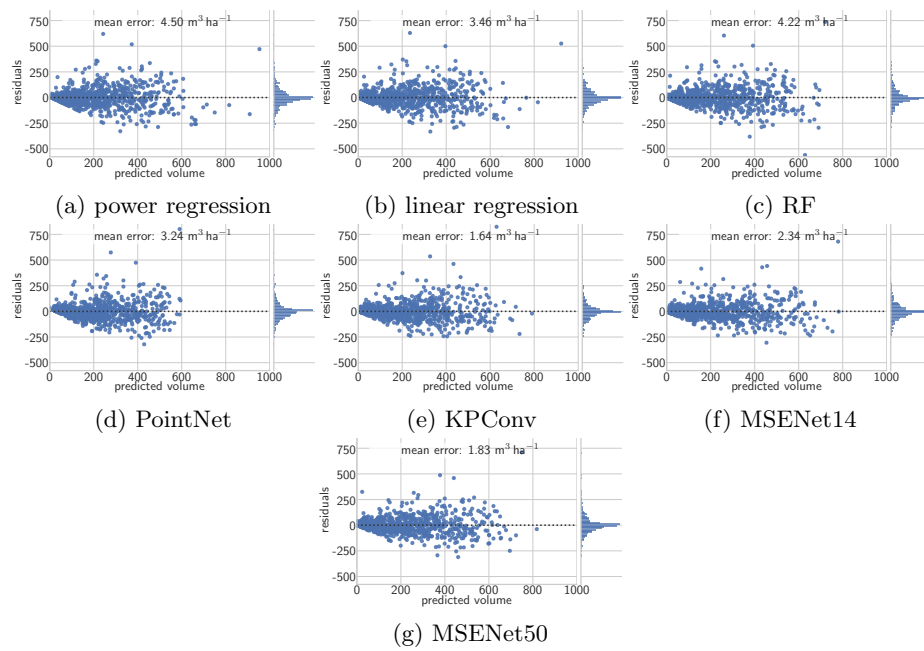
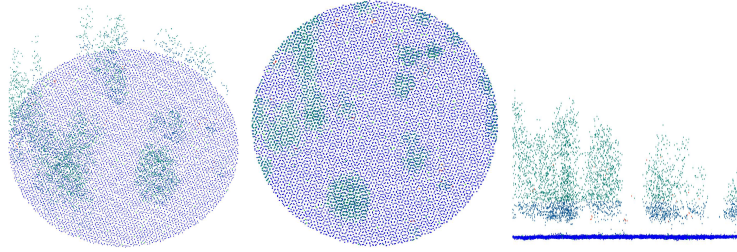
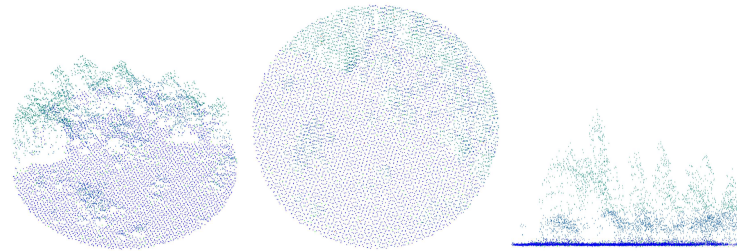


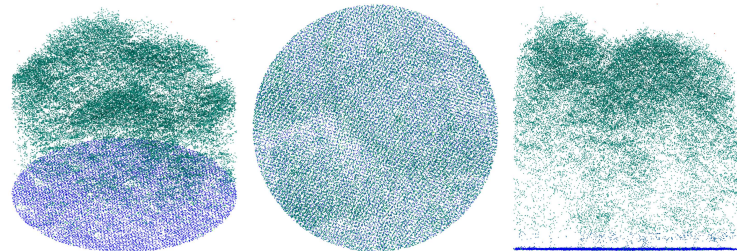
Figure 12: Wood volume residual (left side) and error distribution (right side) plots of the test performance.



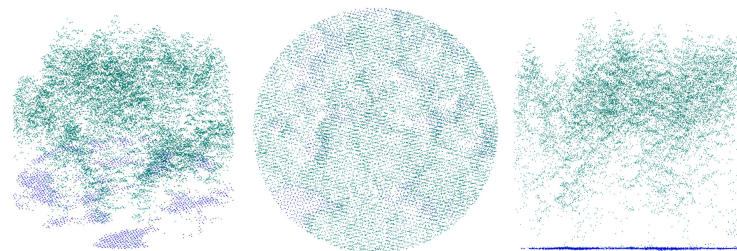
(a) Target: 1.79; MSENNet14: 1.59; KPConv: 3.16; PointNet: 10.17; RF: 8.70, lin. model: 10.42; power model: 11.31



(b) Target: 0.86; MSENNet14: 1.00; KPConv: 3.99; PointNet: 11.31; RF: 7.00, lin. model: 8.09; power model: 9.94



(c) Target: 417.60; MSENNet14: 345.71; KPConv: 381.54; PointNet: 298.25; RF: 285.75, lin. model: 272.74; power model: 270.98



(d) Target: 245.90; MSENNet14: 212.94; KPConv: 273.01; PointNet: 195.50; RF: 216.13, lin. model: 212.38; power model: 217.86



Figure 13: More examples of subplots in each row with three perspectives: isometric front, top, and side view. Each subplots caption contains the measured and estimated biomass in Mg ha^{-1} .

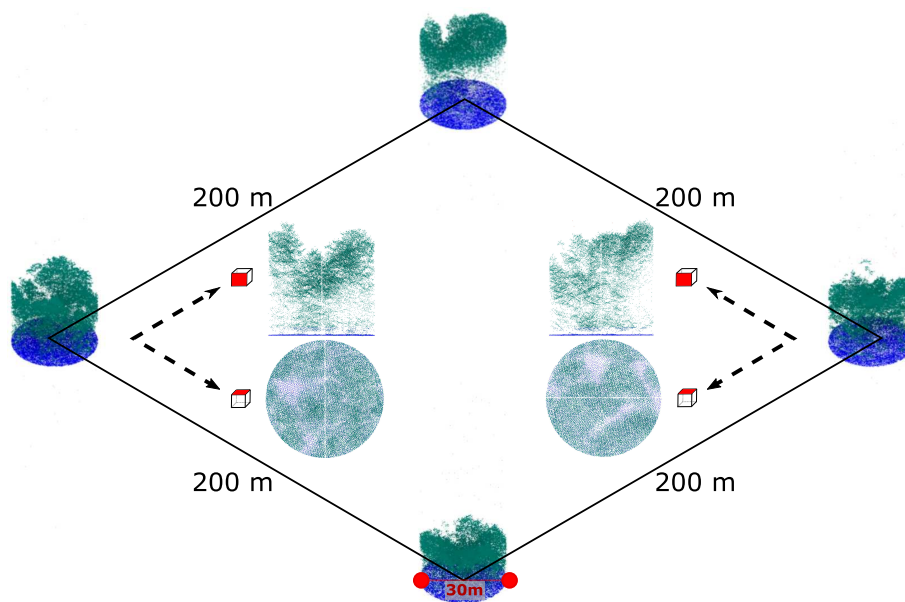


Figure 14: One plot sample from a 2×2 km area as described in Sec. 2.1. Each plot usually contains four subplots in a 200×200 m square. All LiDAR subplots have a diameter of 30 m and their own biomass as well as wood volume measurements.